Thermoelectric properties of a quantum dot coupled to magnetic leads by Rashba spin-orbit interaction

Łukasz Karwacki[1,*] and Józef Barnaś[1,2]

[1]*Institute of Molecular Physics, Polish Academy of Sciences, ul. M. Smoluchowskiego 17, 60-179 Poznań, Poland*
[2]*Faculty of Physics, Adam Mickiewicz University, ul. Umultowska 85, 61-614 Poznań, Poland*

We consider a single-level quantum dot coupled to two leads which are ferromagnetic in general. Apart from tunneling processes conserving electron spin, we also include processes associated with spin flip of tunneling electrons, which appear due to Rashba spin-orbit coupling. Charge and heat currents are calculated within the nonequilibrium Green's function technique. When the electrodes are half metallic (fully spin polarized), the Rashba spin-orbit coupling leads to Fano-like interference effects, which result in an enhanced thermoelectric response. It is also shown that such a system can operate as a heat engine with a remarkable efficiency. Furthermore, the interplay of Rashba spin-orbit coupling and Zeeman splitting due to an external magnetic field is shown to allow controlling of such parameters of the heat engine as the power and efficiency.

I. INTRODUCTION

Thermoelectric properties of nanoscale systems have been the subject of many recent studies in condensed matter physics [1,2]. It has been shown theoretically that high thermoelectric figure of merit, which is a measure of thermoelectric efficiency, can be obtained in zero-dimensional (0D) systems with discrete density of states (DOS) [3], such as quantum dots (QDs) or molecules. The discrete DOS of quantum dots, combined with electrical tunability of their energy levels, lead to strong energy filtering of charge carriers. Furthermore, quantum dots can operate in different transport regimes, from a weakly coupled system to a strongly correlated one. Each regime displays distinct behavior with characteristic energy scales. One of the common characteristic features for both regimes is the sign alternation of the Seebeck coefficient with a gate voltage applied to the dot, which has been verified experimentally [4–7]. This effect results from strongly bipolar transport in quantum dots, where tuning an energy level of the dot (with gate voltage) around the Fermi level of the electrodes filters either holes or electrons. A similar effect can be observed when the time-reversal symmetry is broken due to either external magnetic field or ferromagnetic electrodes. The quantum dots can then filter spin-up or spin-down electrons, which results in spin-dependent transport and spin thermoelectric effects [8–11].

Another important property of QDs, extensively studied theoretically, is a large impact of quantum interference effects on electronic transport in different regimes. One such phenomena, known as Fano effect [12], can occur when one of the interfering waves passes through continuum of states while the other wave passes through a narrow discrete level. In quantum dot systems, this effect can occur when the two waves pass through a broad and a narrow discrete level,

respectively. The Fano effect reveals as characteristic anti-resonances in electrical conductance, and in multiple quantum dot structures can also lead to enhanced spin and charge Seebeck coefficients [13–18].

The most common quantum dots are those based on two-dimensional electron gas (2DEG) confined at the interface between two semiconductors, which makes it relatively easy to control properties of the dots with gate voltages. Alternatively, the dots can be created in one-dimensional (1D) structures such as semiconductor nanowires or carbon nanotubes (CNT) [19–21]. One of the effects that can inevitably arise in such systems due to inversion-symmetry breaking at interfaces or due to curvature of CNT is Rashba spin-orbit coupling (RSOC) [22]. This coupling can be controlled by electrical as well mechanical means [23–27]. The mentioned experimental data show that when QD is embedded is such a structure, coupling between the dot and remaining parts (treated as external leads) can include a spin-orbit contribution. Importantly, both spin-conserving and spin-orbit coupling terms can be tuned externally. The spin-orbit coupling can limit spin coherence due to spin-mixing of transport channels [28–30]. However, the spin reversal due to spin-orbit coupling can be also used to induce quantum interference phenomena. For instance, interference effects in mesoscopic structures with RSOC have been proposed in superconducting tunnel junctions [31] and ring interferometers, where Aharonov-Bohm effect and spin-dependent phase shift between different paths traversed by spin-↑ and spin-↓ electrons appear [32,33]. Theoretical studies of such structures indicate some enhancement of the thermoelectric figure of merit and possibility of pure spin current generation [34,35].

Although many of the above properties have been already studied, mostly in the linear response regime, there have been recently many proposals of quantum-dot-based heat engines, where one needs to go beyond the linear response limit. The heat engine based on a single-level quantum dot coupled to two metallic reservoirs has been theoretically predicted to reach
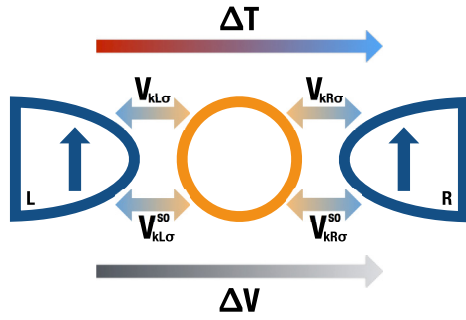
*karwacki@ifmpan.poznan.pl

FIG. 1. Schematic presentation of the quantum dot coupled to two ferromagnetic electrodes. The coupling parameter $V_{\mathbf{k}\beta\sigma}$ ($\beta = L, R$) represents spin-conserving tunneling process, while the parameter $V_{\mathbf{k}\beta\sigma}^{\mathrm{so}}$ represents spin-nonconserving tunneling process due to Rashba spin-orbit coupling. Temperature and electrostatic potential of the left electrode are shifted by ΔT and ΔV in comparison to the right electrode.

either the Curzon-Ahlborn efficiency, i.e., the efficiency of the engine at maximum produced power, or even the Carnot efficiency when a strong coupling between the heat and particle fluxes exists [36–43]. Although this condition occurs for very weakly coupled quantum dots, the possibility of achieving high thermodynamic efficiency in quantum dot systems has been recently verified experimentally [44]. More complex heat engines, based on multiple quantum dots and multiple electrodes, have been proposed as well [45–50]. Conversely, mesoscopic refrigeration schemes have been also proposed [51–53], paving the way to studies on quantum heat transport and its relation with information in the form of Maxwell's demon [54,55].

Here we show that the quantum dot with RSOC can operate as a heat engine with the efficiency that can be controlled not only by position of the dot's energy level and external magnetic field, but also by strength of the RSOC. Moreover, we show that when the quantum dot is coupled to half-metallic electrodes, the RSOC gives rise to the Fano-like interference effect. This effect leads to higher thermoelectric parameters and enhanced efficiency of the heat engine. More complex effects appear when external magnetic field is applied to the system.

The paper is organized as follows. Section II contains a description of the model and of the quantities being considered (charge and heat currents). Basic information on the power produced by a heat engine and the corresponding efficiency is also presented there. Section III presents numerical results obtained for the quantities introduced in Sec. II. A short summary of the paper is presented in Sec. IV.

II. THEORETICAL DESCRIPTION

A. Model

The system under consideration is presented schematically in Fig. 1. The quantum dot is coupled to two electrodes by direct (spin conserving) tunneling and tunneling with Rashba interaction (spin nonconserving). The system can be described by the following Hamiltonian:

$$\hat{H} = \hat{H}_e + \hat{H}_{\mathrm{qd}} + \hat{H}_t^0 + \hat{H}_t^{\mathrm{so}}, \tag{1}$$

where the first term,

$$\hat{H}_e = \sum_{\mathbf{k}\beta\sigma} \varepsilon_{\mathbf{k}\beta\sigma} c_{\mathbf{k}\beta\sigma}^\dagger c_{\mathbf{k}\beta\sigma}, \tag{2}$$

describes the left ($\beta = L$) and right ($\beta = R$) electrodes, which are ferromagnetic in a general case. Magnetic moments of the electrodes are assumed to be parallel, and orientation of the moments determines the quantization axis for the system.

The second term in Hamiltonian Eq. (1) stands for the single-level quantum dot,

$$\hat{H}_{\mathrm{qd}} = \sum_\sigma \varepsilon_\sigma d_\sigma^\dagger d_\sigma + U \hat{n}_\uparrow \hat{n}_\downarrow, \tag{3}$$

where $\varepsilon_\sigma = \varepsilon_d + \hat{\sigma} g \mu_B B/2$, with ε_d being the bare dot's level, $\hat{\sigma}$ defined as $\hat{\sigma} = 1(-1)$ for $\sigma = \uparrow (\downarrow)$, B denoting an external magnetic field, and g and μ_B standing for the Lande factor and Bohr magneton, respectively. In turn, U in Eq. (3) is the Coulomb correlation parameter, while $\hat{n}_\uparrow (\hat{n}_\downarrow)$ is the occupation operator for spin-up (spin-down) electrons.

The last two terms in Eq. (1) describe electron tunneling between the electrodes and quantum dot. One of them, $\hat{H}_t^0$, conserves electron spin in the tunneling processes,

$$\hat{H}_t^0 = \sum_{\mathbf{k}\beta\sigma} V_{\mathbf{k}\beta\sigma} c_{\mathbf{k}\beta\sigma}^\dagger d_\sigma + \text{H.c.}, \tag{4}$$

while the second one, $\hat{H}_t^{\mathrm{so}}$, is due to Rashba interaction and takes the form

$$\hat{H}_t^{\mathrm{so}} = -\sum_{\mathbf{k}\beta\sigma} \left[V_{\mathbf{k}\beta\bar{\sigma}}^{\mathrm{so}} c_{\mathbf{k}\beta\bar{\sigma}}^\dagger (i\hat{\sigma}_x)_{\sigma\bar{\sigma}} d_\sigma \right] + \text{H.c.}, \tag{5}$$

where $\hat{\sigma}_x$ denotes the x component of the vector of Pauli matrices. The latter term is responsible for electron spin-flips in tunneling processes. When the leads are half metallic, the above-introduced model is equivalent to a spinless two-level quantum dot model [56,57].

B. Currents and heat engine

The electric current j_e flowing in the biased system from left to right can be described by the formula

$$j_e = \frac{e}{\hbar} \int \frac{d\varepsilon}{2\pi} [f_L(\varepsilon) - f_R(\varepsilon)] T(\varepsilon), \tag{6}$$

where e denotes the electron charge ($e < 0$), $f_{L(R)}$ is the Fermi-Dirac distribution in the left (right) electrode, while $T(\varepsilon)$ is the total transmission function, $T(\varepsilon) = T_\uparrow(\varepsilon) + T_\downarrow(\varepsilon)$, whose explicit form will be derived in the next subsection. The spin-dependent transmission $T_{\uparrow(\downarrow)}(\varepsilon)$ is defined as the total transmission from the spin-σ chanel of one electrode to both spin channels in the second electrode.

Since the dot is coupled, in general, to ferromagnetic electrodes, the charge current may be accompanied with a spin current. However, we assume no spin accumulation in the leads (no spin voltage and no spin thermoelectric effects), and therefore we do not consider the spin currents.

The charge current is also associated with energy flow, and the corresponding energy current is given by the formula

$$j_E = \frac{1}{\hbar} \int \frac{d\varepsilon}{2\pi} \varepsilon [f_L(\varepsilon) - f_R(\varepsilon)] T(\varepsilon). \tag{7}$$

The energy current is conserved, but the associated heat current is not conserved in nonequilibrium situations. According to the second law of thermodynamics, the energy increase of the dot is equal to the heat flowing into it and the work done on it. The heat current flowing from the left electrode can be written as

$$j_h^L = \frac{1}{\hbar} \int \frac{d\varepsilon}{2\pi} (\varepsilon - \mu_L)[f_L(\varepsilon) - f_R(\varepsilon)] T(\varepsilon), \qquad (8)$$

where μ_L is the electrochemical potentials of the left electrode. A similar formula holds for the heat flowing from the right electrode to the dot. These heat currents are generally different. The heat current is conserved only in quasiequilibrium state (infinitesimally small deviation from equilibrium).

In the linear response regime (quasiequilibrium situation), the charge and heat currents driven by small bias voltage δV and temperature difference δT can be written in the following form:

$$\begin{bmatrix} j_e \\ j_h \end{bmatrix} = \begin{bmatrix} e^2 L_0 & \frac{e}{T} L_1 \\ e L_1 & \frac{1}{T} L_2 \end{bmatrix} \begin{bmatrix} \delta V \\ \delta T \end{bmatrix}, \qquad (9)$$

where

$$L_i = \frac{1}{\hbar} \int \frac{d\varepsilon}{2\pi} (\varepsilon - \mu)^i \left(-\frac{\partial f_0}{\partial \varepsilon} \right) T(\varepsilon) \qquad (10)$$

for $i = 0, 1, 2$. Here, f_0 is the Fermi-Dirac distribution function in equilibrium (corresponding to the chemical potential μ). Note, according to our definitions, $\delta V = V_L - V_R = (\mu_L - \mu_R)/e$ and $\delta T = T_L - T_R$. Here, T_L (T_R) stands for the temperature of the left (right) lead. Similarly, V_L (V_R) and μ_L (μ_R) stand for the electric and chemical potentials in the left (right) lead, respectively. The electrical conductance, G, can then be calculated as $G = e^2 L_0$, while the thermopower S is given by the formula $S = -\frac{\delta V}{\delta T} = \frac{1}{eT} \frac{L_1}{L_0}$. The linear-response G and S determine the corresponding power factor P_0 as $P_0 = G S^2$.

When the system is supposed to work as a heat engine, the linear response regime is then not sufficient and one needs to go beyond this limit. In other words, δV and δT should be replaced by a finite (not small) ΔV and ΔT, where transport characteristics are nonlinear. The charge and heat currents cannot then be calculated from Eqs. (9), but instead one should use Eqs. (6) and (8). Note, the conductance $G = j_e / \Delta V$, the thermopower S,

$$S = -\frac{\Delta V}{\Delta T}, \qquad (11)$$

and the corresponding power factor $P_0 = G S^2$ depend then on the voltage ΔV.

The work done on the system per unit time is $j_e \Delta V$. When the system operates as a heat engine, then it generates a finite power,

$$P = -j_e \Delta V, \qquad (12)$$

where ΔV is the voltage applied to counteract the thermally induced current. The maximal power generated by the engine can be described with the following formula [58]:

$$P_{\max} = G V_{\max}^2 = \frac{1}{4} G V_b^2 = \frac{1}{4} P_0 (\Delta T)^2, \qquad (13)$$

where $V_{\max} = V_b/2$ is the voltage for which power is maximal, while $V_b = -S\Delta T$ is the stopping (or blocking) voltage.

Efficiency of the heat engine is defined as

$$\eta = \frac{P}{j_h^L}. \qquad (14)$$

The second law of thermodynamics introduces the upper limit on the efficiency in the form of Carnot efficiency,

$$\eta_C = \frac{\Delta T}{T}, \qquad (15)$$

where T is the temperature of the hotter (here left) reservoir. Additionally, for realistic heat engines, when one considers device output at maximal power, a Curzon-Ahlborn efficiency can be introduced [36],

$$\eta_{CA} = 1 - \sqrt{1 - \eta_C}, \qquad (16)$$

which for strongly coupled particle and energy currents in the linear response acquires a finite value, $\eta_{CA} \approx \eta_C/2 + \mathcal{O}(\eta_C^2)$ [37].

C. Method

To find the charge and heat currents introduced above, one needs to know the transmission coefficient $T(\varepsilon) = T_\uparrow(\varepsilon) + T_\downarrow(\varepsilon)$. Since the temperature assumed in the paper is much larger than the corresponding Kondo temperature, one can treat the Coulomb interaction between electrons residing on the dot in the mean field approximation. Then, one finds

$$T_\sigma(\varepsilon) = \mathrm{Tr}\{\mathbf{\Gamma}_{L\sigma} \mathbf{G}^r(\varepsilon) \mathbf{\Gamma}_R \mathbf{G}^a(\varepsilon)\} \qquad (17)$$

for $\sigma = \uparrow, \downarrow$. This transmission coefficient can be understood as coupling of spin σ state from the left electrode to both spin states of the right electrode, i.e., it can be decomposed into spin-conserving transmission, and transmission with spin reversal due to the spin-orbit coupling, i.e,. spin-mixing transmission coefficient. The $T_\sigma(\varepsilon)$ coefficient can be equivalently defined as coupling of both spin states from left electrode to a selected spin state from the right electrode.

The Green's functions can be derived from the Dyson equation,

$$\mathbf{G}^{r(a)} = \left[\left(\mathbf{g}_0^{r(a)} \right)^{-1} - \mathbf{\Sigma}^{r(a)} \right]^{-1}, \qquad (18)$$

with $\mathbf{g}_0^{r(a)}$ being the Green's function of the corresponding isolated dot, whose diagonal elements are defined as follows:

$$g_{0\sigma\sigma}^{r(a)} = \frac{1 - n_{\bar{\sigma}}}{\varepsilon - \varepsilon_\sigma \pm i0^+} + \frac{n_{\bar{\sigma}}}{\varepsilon - \varepsilon_\sigma - U \pm i0^+}, \qquad (19)$$

where $n_\sigma = \langle \hat{n}_\sigma \rangle$. The self-energy $\mathbf{\Sigma}^{r(a)}$ takes the following form:

$$\mathbf{\Sigma}^{r(a)} = \mp \frac{i}{2} \sum_\beta \mathbf{\Gamma}_\beta, \qquad (20)$$

where $\mathbf{\Gamma}_\beta = \mathbf{\Gamma}_{\beta\uparrow} + \mathbf{\Gamma}_{\beta\downarrow}$. The coupling matrices are defined as

$$\mathbf{\Gamma}_{\beta\uparrow} = \begin{bmatrix} \Gamma_{\beta\uparrow\uparrow} & -i\sqrt{\Gamma_{\beta\uparrow\uparrow} \Gamma_{\beta\uparrow\uparrow}^{so}} \\ i\sqrt{\Gamma_{\beta\uparrow\uparrow} \Gamma_{\beta\uparrow\uparrow}^{so}} & \Gamma_{\beta\uparrow\uparrow}^{so} \end{bmatrix} \qquad (21)$$

for spin $\sigma = \uparrow$, and

$$\mathbf{\Gamma}_{\beta\downarrow} = \begin{bmatrix} \Gamma^{\mathrm{so}}_{\beta\downarrow\downarrow} & i\sqrt{\Gamma_{\beta\downarrow\downarrow}\Gamma^{\mathrm{so}}_{\beta\downarrow\downarrow}} \\ -i\sqrt{\Gamma_{\beta\downarrow\downarrow}\Gamma^{\mathrm{so}}_{\beta\downarrow\downarrow}} & \Gamma_{\beta\downarrow\downarrow} \end{bmatrix} \quad (22)$$

for spin $\sigma = \downarrow$. In the above matrices $\Gamma_{\beta\sigma\sigma} = 2\pi\langle|V_{\mathbf{k}\beta\sigma}|^2\rangle\rho_{\beta\sigma}$ and $\Gamma^{\mathrm{so}}_{\beta\sigma\sigma} = 2\pi\langle|V^{\mathrm{so}}_{\mathbf{k}\beta\sigma}|^2\rangle\rho_{\beta\sigma}$, with $\rho_{\beta\sigma}$ denoting the spin-dependent DOS in the βth lead. In the following, we introduce the parameters Γ_β through the relation $\Gamma_{\beta\sigma\sigma} = (1 + \hat{\sigma} p_\beta)\Gamma_\beta$, where p_β is the spin polarization of the lead β. We also introduce the parameter q defined as $\Gamma^{\mathrm{so}}_{\beta\sigma\sigma} = q\Gamma_{\beta\sigma\sigma}$. This parameter describes the relative strength of RSOC. Accordingly, the parameters Γ_L, Γ_R, p_L, p_R, and q will be used to describe coupling of the dot to both leads.

To obtain the dot's mean occupation for spin-σ electrons, $n_\sigma = -i\int d\varepsilon/2\pi\, G^<_\sigma$, we use the Keldysh formula,

$$\mathbf{G}^< = i\mathbf{G}^r(f_L\mathbf{\Gamma}_L + f_R\mathbf{\Gamma}_R)\mathbf{G}^a, \quad (23)$$

where $\mathbf{G}^<$ is the correlation (lesser) Green's function.

III. NUMERICAL RESULTS

In this section, we present numerical results. The section is divided into three parts: in the first one we consider mean occupation of the dot by spin-$\uparrow$ and spin-$\downarrow$ electrons in the absence and presence of an external magnetic field. Thermoelectric effects and heat engine in the limit of zero magnetic field are analyzed in the second part, while the influence of a finite magnetic field is considered in the third part. In all calculations, we assumed symmetrical coupling of the dot to both leads, $\Gamma_L = \Gamma_R = \Gamma$. Apart from this, we assumed $U = 10\Gamma$ and $k_B T = 0.5\Gamma$ (unless otherwise specified), where $\Gamma = 0.01D$ is used as the energy unit, with D being the leads' half-bandwidth. Note that the temperatures considered here are much higher than the corresponding Kondo temperature. The problem of Kondo correlations in the model under consideration was investigated elsewhere [57].

A. Mean occupations and average spin

To better understand complex behavior of the thermoelectric effects in quantum dots coupled to half-metallic leads *via* tunneling with Rashba spin-orbit interaction, it is helpful to analyze first the mean occupation of the dot by spin-$\uparrow$ and spin-$\downarrow$ electrons as well as the dot's average spin. Due to Coulomb correlations, these parameters have a significant impact on charge and spin transport. In Fig. 2, we show these parameters as a function of the quantum dot's energy level for selected values of the RSOC (described by the parameter q), fixed values of magnetic field $g\mu_B B$, and half-metallic leads, $p_L = p_R = 1$.

The occupation numbers and the dot's average spin S_z in the absence of external magnetic field, $g\mu_B B = 0$, are shown in Figs. 2(a), 2(e) and 2(i), respectively. When the RSOC is absent, $q = 0$, the dot can be occupied by a single spin-$\uparrow$ electron only. However, when the RSOC is nonzero, spin of an electron can rotate when tunneling to the dot, and the quantum dot can be occupied by a spin-$\downarrow$ electron as well. Accordingly, the dot can then be either empty, or singly occupied (by a spin-$\uparrow$ or spin-$\downarrow$ electron), or occupied by two electrons (spin-$\uparrow$ and
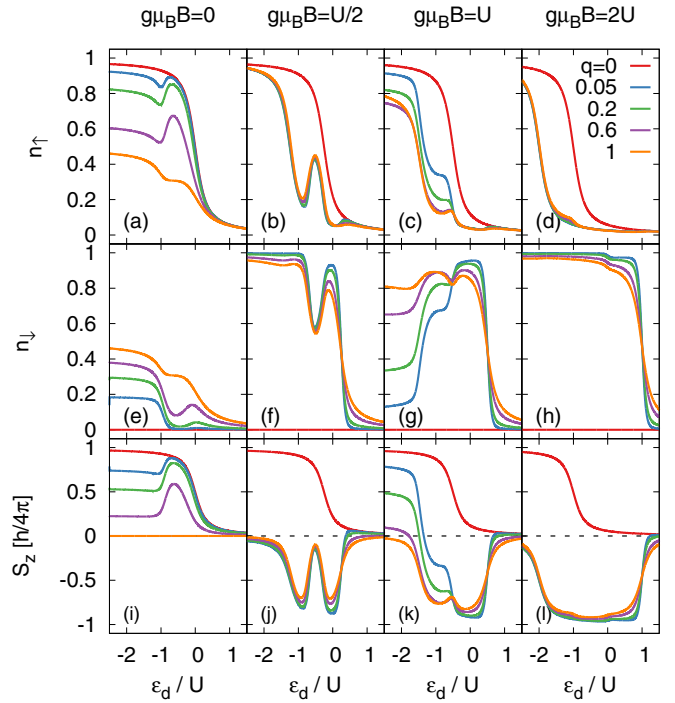

FIG. 2. Mean occupation of the dot by a spin-$\uparrow$ electron, $n_\uparrow$, (a)–(d), by spin-$\downarrow$ electron, $n_\downarrow$, (e)–(h), and the average spin of the dot, $S_z/(\hbar/2) \equiv n_\uparrow - n_\downarrow$, (i)–(l), presented as a function of the dot's bare energy level, ε_d, and calculated in the linear response regime for indicated values of the Rashba spin-orbit parameter q and Zeeman splitting $g\mu_B B$. Other parameters: $p_L = p_R = 1$, $k_B T = 0.5\Gamma$, and $U = 10\Gamma$. The dashed line indicates $S_z = 0$.

spin-$\downarrow$). Due to a nonzero occupation of the dot by a spin-$\downarrow$ electron, the average spin S_z of the dot is adequately reduced. In the case of $q = 1$, the dot can be occupied equally by spin-$\uparrow$ and spin-$\downarrow$ electrons, which results in zero average spin, irrespective of the dot's energy level.

The occupation numbers in the presence of a magnetic field are shown in Figs. 2(b), 2(f) and 2(j) for $g\mu_B B = U/2$; in Figs. 2(c), 2(g) and 2(k) for $g\mu_B B = U$; and in Figs. 2(d), 2(h) and 2(l) for $g\mu_B B = 2U$. For $q = 0$, the situation is qualitatively similar to that in the absence of magnetic field, i.e., only a single spin-$\uparrow$ electron can appear on the dot, so the average spin of the dot is positive. Some shift of the curves toward lower energy of the dot's levels with increasing B results from the Zeeman splitting of the energy level. Increase in the RSOC (parameter q) leads to remarkable changes in the dependence of the occupation numbers $n_\uparrow$ and $n_\downarrow$ (and thus also of the mean dot's spin) on the dot's bare energy level ε_d. These changes result from two factors: (i) Zeeman splitting of the dot's energy level and (ii) ratio of the spin-conserving and spin-reversal tunneling rates. The average spin of the dot is now predominantly negative, though in certain regions of the level energy the average spin may be positive.

B. Heat engine for $B = 0$

In this section, we show numerical results on a quantum dot-based heat engine in the absence of external magnetic field, $B = 0$. First, we analyze the electrical conductance,
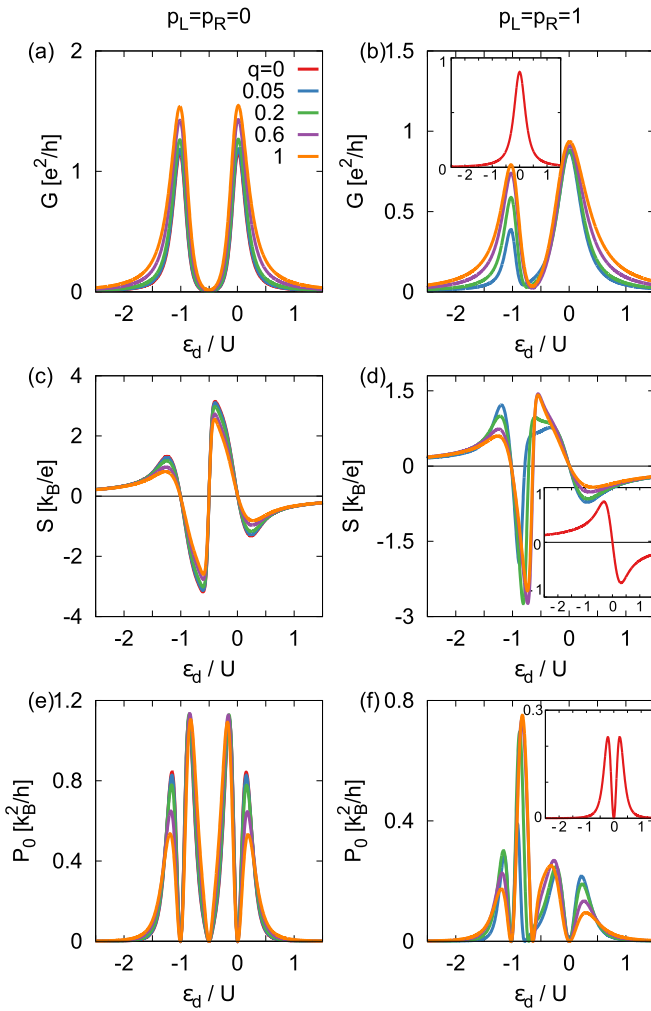
FIG. 3. Electrical conductance, G, (a) and (b), Seebeck coefficient, S, (c) and (d), and power factor, P_0, (e) and (f), presented as a function of the dot's energy level, ε_d, and calculated in the linear response regime for indicated values of the parameter q and polarization of the leads. Other parameters: $g\mu_B B = 0$, $k_B T = 0.5\Gamma$, and $U = 10\Gamma$. Insets show the case of $q = 0$ for $p_L = p_R = 1$.

thermopower, and power factor in the linear response regime, and then the power and efficiency in the nonlinear regime. One should note that thermoelectric properties of single-level quantum dots in the absence of Rashba coupling have been already investigated theoretically for different magnetic configurations of the leads, see, e.g., Ref. [9]. The conductance, thermopower, and power factor in a nonmagnetic case, $p_L = p_R = 0$, presented in Figs. 3(a), 3(c), and 3(e) as a function of the dot's energy level, behave in a similar way as the results presented in earlier works. However, they additionally show the impact of RSOC. More specifically, Fig. 3(a) shows that the two-peak structure of the conductance, i.e., the resonant peak and its Coulomb counterpart, is conserved when the Rashba coupling is nonzero. However, both peaks become slightly broadened for $q > 0$ due to enhanced effective coupling between the dot and the leads. Apart from this, the conductance maxima increase with the parameter q due to enhanced total transmission owing to the spin-rotation processes. Note that the conductance does not achieve the conductance quantum $2e^2/h$ due to a finite

temperature. In turn, the Seebeck coefficient shown in Fig. 3(c) changes sign at the resonances, i.e., for $\varepsilon_d = 0$ and $\varepsilon_d = -U$, as well as in the particle-hole symmetry point, $\varepsilon_d = -U/2$. In the definition used here, the positive (negative) Seebeck coefficient corresponds to transport mediated by holes (electrons). Thus, this figure shows that the character of transport carriers is retained for $q > 0$. A weak drop in the thermopower with increasing q results from increasing role of spin-reversal transmission. Due to this decrease in the Seebeck coefficient, the power factor shown in Fig. 3(e) also decreases, as it is proportional to S^2.

In the case of half-metallic leads, $p_L = p_R = 1$, the conductance shown in Fig. 3(b) behaves differently. For $q = 0$, there is only one peak in the conductance at $\varepsilon_d = 0$, which corresponds to tunneling of spin-↑ electrons through the bare dot's level (there are no spin-↓ electrons in the leads). For a small nonzero value of q, the peak in conductance for $\varepsilon_d = 0$ is broadened, but an additional peak emerges at $\varepsilon_d = -U$. Moreover, the conductance spectrum is now asymmetric, which is typical of the Fano antiresonance. The increasing rate of spin-flip processes with increasing q leads to an increase in electrical conductance. It is worth noting, however, that the maximal value of the conductance is comparable to that in the corresponding nonmagnetic case. The thermopower for $q = 0$ vanishes only when $\varepsilon_d = 0$, and is antisymmetric with respect to this point, as shown in Fig. 3(d). In turn, the thermopower for $q > 0$ is neither symmetric nor antisymmetric with respect to the particle-hole symmetry point, $\varepsilon_d = -U/2$. This results from the contribution due to spin-reversal tunneling. Moreover, when the strength of RSOC increases, the thermopower becomes higher. The maximal value of the thermopower is negative, which indicates particle(electron)-like character of transport. This strong dependence of the thermopower on the type of carriers and Coulomb interaction has a significant influence on the position of the dot's energy level where the Seebeck coefficient changes sign. This change occurs, as has been already discussed above, for $\varepsilon_d = 0$, U, and $\varepsilon_\pm$, where

$$\varepsilon_\pm = \frac{1}{1+q}[1 - n_\downarrow - q(1 - n_\uparrow)]U$$

$$\pm \frac{1}{1+q}\sqrt{(n_\downarrow - 1 + (n_\uparrow - 1)q)(n_\downarrow + n_\uparrow q)U^2}. \quad (24)$$

Since the power factor, shown in Fig. 3(f), reflects the structure of both thermopower and conductance, it is symmetric with respect to $\varepsilon_d = 0$ for $q = 0$, and strongly asymmetric for $q > 0$. For $q > 0$, the power factor achieves the largest value for $\varepsilon_d \approx -0.75U$, where the corresponding Seebeck coefficient is maximal. It is worth noting that the power factor for $q = 0$ is significantly smaller when compared to that for $q > 0$.

Temperature dependence of the linear conductance, thermopower, and power factor is shown in Fig. 4 for two positions of the dot's energy level, $\varepsilon_d = -0.9U$ and $\varepsilon_d = -0.25U$. Note, $\varepsilon_d = -0.9U$ ($\varepsilon_d = -0.25U$) corresponds to the Rashba-induced (background) peak in Fig. 3(b). Therefore, the conductance shown in Fig. 4(a) for $\varepsilon_d = -0.9U$ is small at low temperatures for $q = 0$, and achieves remarkable values when $k_B T > \Gamma$. When $q > 0$, the conductance displays a more complex behavior. In particular, the Rashba-induced transport becomes activated so the conductance may be nonzero also
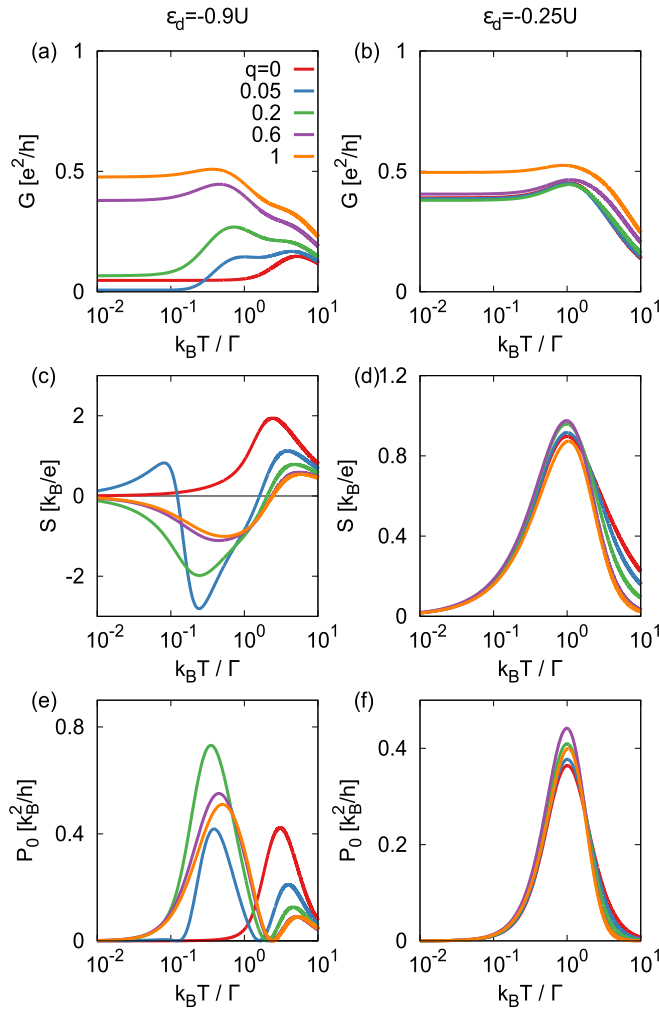
FIG. 4. Electrical conductance, G, (a) and (b), Seebeck coefficient, S, (c) and (d), and power factor, P_0, (e) and (f), presented as a function of temperature, $k_B T$ (in logarithmic scale), and calculated in the linear response regime for indicated values of parameter q and the dot's energy level $\varepsilon_d = -0.9U$ (left column) and $\varepsilon_d = -0.25U$ (right column). Other parameters: $p_L = p_R = 1$, $g\mu_B B = 0$, and $U = 10\Gamma$.

at low temperatures. However, due to the Fano antiresonance, the conductance vanishes at low temperatures, see, e.g., the curve for $q = 0.05$ at $k_B T < 0.1\Gamma$. When q increases, position of the antiresonance shifts toward lower energies, and at low temperatures the conductance achieves a constant value. On the other hand, for the background channel, $\varepsilon_d = -0.25U$, the conductance shown in Fig. 4(b) varies rather weakly with increasing q, since the dominant contribution comes from the spin-↑ peak, which is present even for $q = 0$. We note that the Fano antiresonance appears here due to interference of waves transmitted via the spin-↑ and spin-↓ discrete levels. In the former case, the transmission appears due to spin-conserving tunneling processes, while in the latter one due to spin-orbit interaction. In the second case, the electron spin rotates from spin-↑ to spin-↓ when the electron tunnels from the left lead to the dot and then from spin-↓ to spin-↑ when the electron tunnels from the dot to the right lead. The corresponding temperature dependence of the thermopower for the Rashba-induced ($\varepsilon_d = -0.9U$) and background

($\varepsilon_d = -0.25U$) channels is shown in Figs. 4(c) and 4(d), respectively. In the former case, the thermopower for $q = 0$ is positive and small for $k_B T < \Gamma$, while for $k_B T > \Gamma$ it increases and achieves a maximal value for $k_B T \approx 2.5\Gamma$. This peak remains for $q > 0$, but its height decreases with increasing q and its position shifts toward higher temperatures. Moreover, due to the contribution from the Rashba-induced channel, the variation of the thermopower with temperature then differs remarkably from that for $q = 0$. Apart from this, the energy levels where the thermopower changes sign depend on the average occupation numbers, see Eq. (24), which depend on temperature, in general. All this leads to sign reversal of the thermopower with decreasing temperature, which takes place twice for small values of q [see the curve for $q = 0.05$ in Fig. 4(c)] and once for larger values of q. For $\varepsilon_d = -0.25U$, the thermopower is dominated by the background channel, and therefore it is only weakly dependent on q, see Fig. 4(d). The power factor is shown in Fig. 4(e) for $\varepsilon_d = -0.9U$ and in Fig. 4(f) for $\varepsilon_d = -0.25U$. It reaches maximum values at temperatures which approximately correspond to maximum values of the thermopower. Interestingly, the maximum value of P_0 is for $q = 0.2$ and not for $q = 0.05$ where the Seebeck coefficient is larger. This is due to the fact that the conductance for $q = 0.05$ in the relevant temperature range is smaller than for $q = 0.2$.

The key parameters that characterize a heat engine are the generated power P and the efficiency η. The power generated in the system under consideration, working as a heat engine, is shown in Fig. 5 as a function of $|e\Delta V|$ and the dot's energy level, ε_d, for indicated values of q and fully polarized leads, $p_L = p_R = 1$. The power was calculated from Eq. (11), in which ΔV is a voltage applied to counteract the thermally induced current j_e. This means that ΔV and j_e have opposite signs when the system operates as a heat engine. The first row from the top in Fig. 5 corresponds to positive ΔV (negative $e\Delta V$) while the second row to negative ΔV (positive $e\Delta V$).

For $q = 0$, shown in Figs. 5(a) and 5(f), the power exhibits a single relatively broad peak, which for positive ΔV appears for $\varepsilon_d > 0$ [Fig. 5(a)], while for negative ΔV appears for $\varepsilon_d < 0$ [Fig. 5(f)]. Since the Coulomb blockade peaks are absent for $q = 0$ due to full spin polarization of both leads (double occupancy of the dot is forbidden), there is only one peak for positive and one for negative voltage. When $\varepsilon_d > 0$, then the current is dominated by electrons, while for $\varepsilon_d < 0$ it is dominated by holes. Accordingly, the currents in these two regimes have opposite signs and thus the voltages against these currents also have opposite signs. Note, the corresponding Seebeck coefficients in these two regimes have opposite signs, too. The power vanishes for $\varepsilon_d = 0$, because the corresponding Seebeck coefficient is equal to zero, so the voltage disappears.

The suppression of double occupancy of the dot is lifted when the spin-orbit channel for transmission is open, which appears for nonzero values of q. The Coulomb peaks in transport characteristics are then clearly seen, as already mentioned above. As a result, a second peak in the power appears for positive as well as for negative ΔV. Indeed, for a nonzero but small q, an additional peak in the power appears at $\varepsilon_d < 0$ for both $\Delta V > 0$ and $\Delta V < 0$, as shown in Figs. 5(b) and 5(g) for $q = 0.05$.
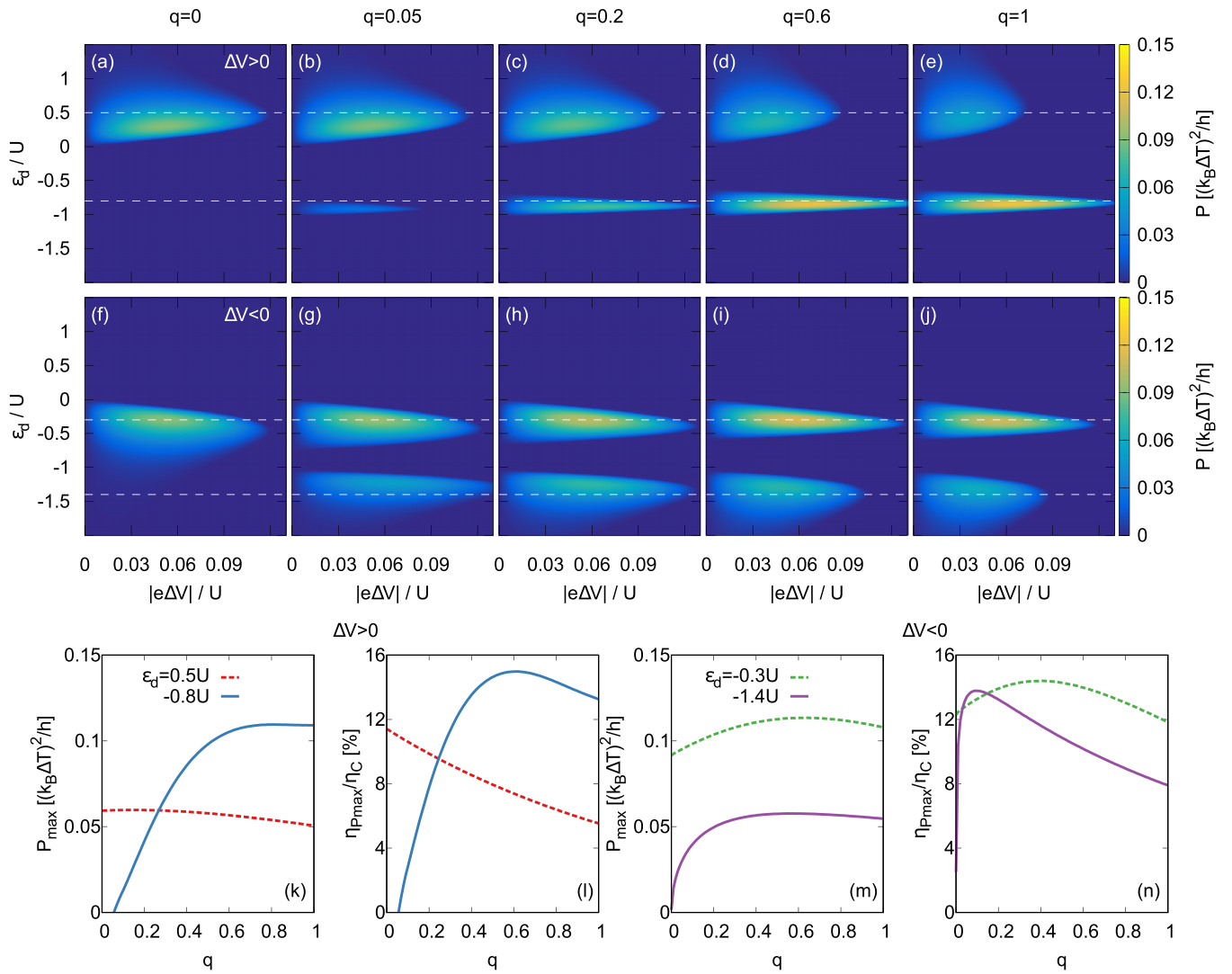
FIG. 5. Power, P, for $\Delta V > 0$ (a)–(e) and $\Delta V < 0$ (f)–(j) as a function of the dot's energy level, ε_d, and applied bias voltage, $|e\Delta V|$, for indicated values of the parameter q. Maximal power, $P_{\max}$, and normalized efficiency at maximal power, $\eta_{P_{\max}}$, as a function of the parameter q for indicated dot's energy levels [marked also by the white dashed lines in (a) to (j)] and for $\Delta V > 0$ (k), (l) and $\Delta V < 0$ (m), (n). Other parameters: $p_L = p_R = 1$, $g\mu_B B = 0$, $U = 10\Gamma$, $k_B T = k_B T_R = 0.5\Gamma$, and $\Delta T = 2T$.

Intensity of the peaks changes with increasing q. For $\Delta V > 0$, intensity of the additional peak (absent for $q = 0$) increases with increasing q, whereas the intensity of the peak existing at $q = 0$ decreases with increasing q, see Figs. 5(a) to 5(e). In turn, for $\Delta V < 0$, see Figs. 5(f) to 5(j), intensity of the additional peak is rather low, while the intensity of the peak existing also for $q = 0$ slightly increases with increasing q.

It is known that for practical purposes a heat engine should work with the highest efficiency when the power is maximal. Figures 5(k) to 5(n) show the maximal power and the efficiency at maximal power, both as a function of the parameter q and for indicated positions of the dot's energy level. These positions are indicated by white dashed lines in Figs. 5(a)–5(j), and correspond to the background and Rashba-induced channels. For $\varepsilon_d = 0.5U$ and $\Delta V > 0$, both maximal power and the efficiency at maximal power are largest for $q = 0$ and then both decrease with increasing q. In the vicinity of the interference-induced resonance, i.e., for $\varepsilon_d = -0.8U$, there is no power generated when $q \lesssim 0.06$. Above this threshold, the

maximal power increases and saturates when q approaches the limit $q = 1$, whereas the efficiency at maximal power reaches a maximum for $q \approx 0.6$. For $\Delta V < 0$ and $\varepsilon_d = -0.3U$, both the maximal power and the corresponding efficiency are weakly dependent on q, taking maximal values for $q \approx 0.5$. For $\varepsilon_d \approx -1.4U$, the efficiency decreases monotonically with increasing q while the maximal power saturates for $q \gtrsim 0.3$. The maximal efficiency for both voltage polarities, however, is lower than the appropriate Carnot efficiency and lower than the Curzon-Ahlborn efficiency, $\eta_{CA}/\eta_C \approx 0.64$.

C. Heat engine for $B \neq 0$

For $B \neq 0$ and nonmagnetic leads, $p_L = p_R = 0$, the electrical conductance shown in Fig. 6(a) as a function of the dot's energy level ε_d displays two additional peaks due to a relatively large Zeeman splitting, $g\mu_B B = 0.6U$. The conductance is symmetric with respect to the particle-hole symmetry point, $\varepsilon_d = -U/2$. The increase in q leads to an increase in
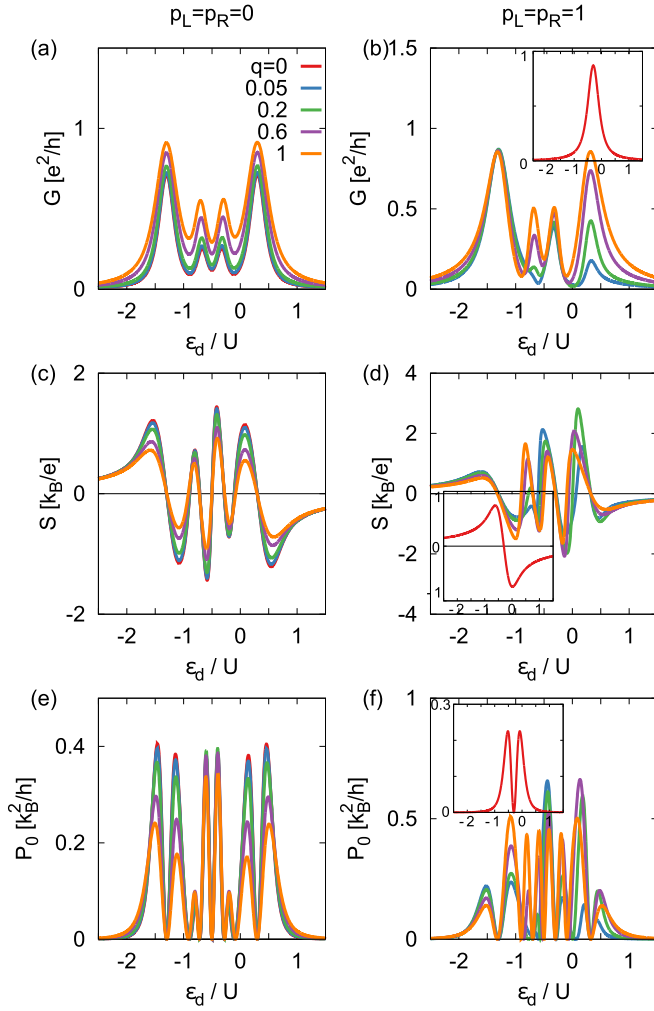
FIG. 6. Linear conductance, G, (a), (b), Seebeck coefficient, S, (c), (d), and power factor, P_0, (e), (f), as a function of the dot's bare energy level, ε_d, for indicated values of the parameter q, and for nonmagnetic (left column) and half-metallic (right column) leads. Other parameters: $g\mu_B B = 0.6U$, $k_B T = 0.5\Gamma$, and $U = 10\Gamma$. Insets show the case of $q = 0$ for $p_L = p_R = 1$.

conductance due to the spin-mixing processes already discussed in the previous section. In turn, the thermopower shown in Fig. 6(c) changes sign two times more than in the case of $B = 0$. Such a behavior is typical for a multilevel system, so we will not discuss it in more detail. With increasing q, the points where the Seebeck coefficient vanishes are slightly shifted away from the points where S vanishes for $q = 0$, except for the particle-hole symmetry point, which is preserved. The corresponding power factor is shown in Fig. 6(e). Since the number of the points where the thermopower vanishes is now larger, the variation of the power factor with the dot's energy level is more complex, i.e., the number of peaks is larger. Heights of these peaks, however, decrease with increasing parameter q due to decreasing thermopower.

The conductance, thermopower, and power factor in the case of half-metallic leads are shown in Figs. 6(b), 6(d) and 6(f). Since there is only one spin channel in the leads, only one component of the Zeeman-split level is then active in transport for $q = 0$, and therefore only one peak appears in the

conductance when Rashba coupling vanishes. Because energy of the spin-↑ level is shifted up by $g\mu_B B/2$ due to Zeeman energy, the corresponding peak appears for $\varepsilon_d = -g\mu_B B/2$. However, a more complex conductance spectrum emerges when $q > 0$. First, both components of the Zeeman-split level contribute to transport. Second, the Coulomb counterparts also appear as now two electrons of opposite spins can reside in the dot.

In turn, the corresponding thermopower for $q = 0$ changes sign only for $\varepsilon_d = \varepsilon_\uparrow$, as follows from the inset in Fig. 6(d). For $q > 0$, behavior of the thermopower with the dot's energy level is more complex and is correlated with the corresponding conductance spectra, as already discussed before. Since the power factor, shown in Fig. 6(f), is determined by both conductance and thermopower, it is evident that the power for $B \neq 0$ can be generated in a range of the bare dot's level energy, which is broader than that for $B = 0$. However, the dependence on q is nonmonotonic, mainly due to nonmonotonic variation of the thermopower with q. Nonetheless, for different strengths
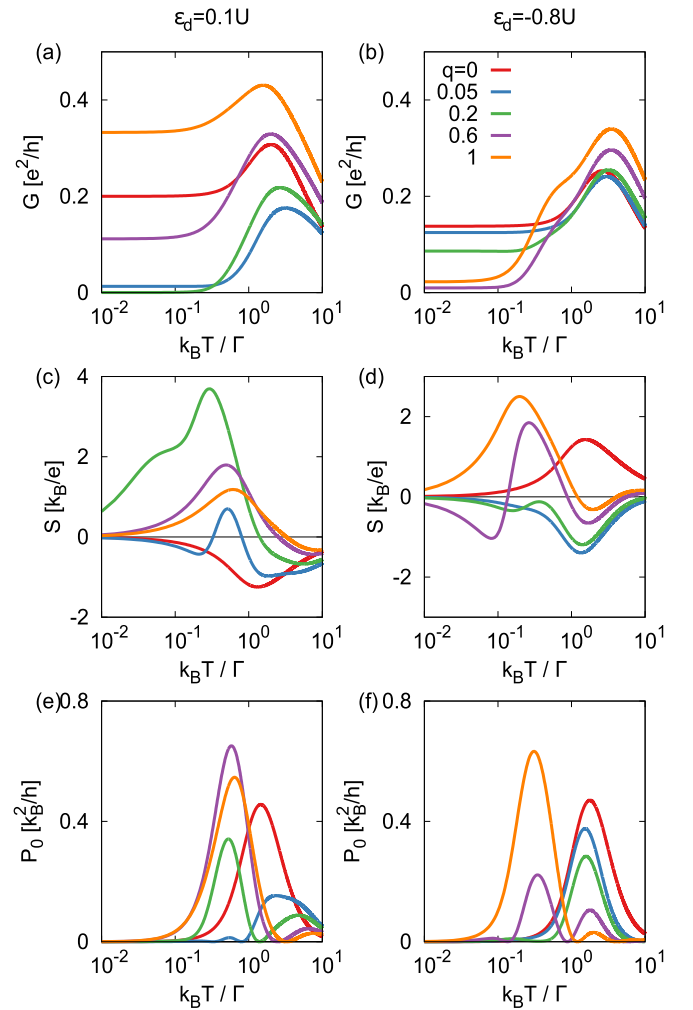

FIG. 7. Linear conductance, G, (a) and (b), Seebeck coefficient, S, (c) and (d), and power factor, P_0, (e) and (f), as a function of temperature, $k_B T$ (in logarithmic scale), for indicated values of the parameter q, and for $\varepsilon_d = 0.1U$ (left column) and $\varepsilon_d = -0.8U$ (right column). Other parameters: $p_L = p_R = 1$, $g\mu_B B = 0.6U$, $k_B T = 0.5\Gamma$, and $U = 10\Gamma$.
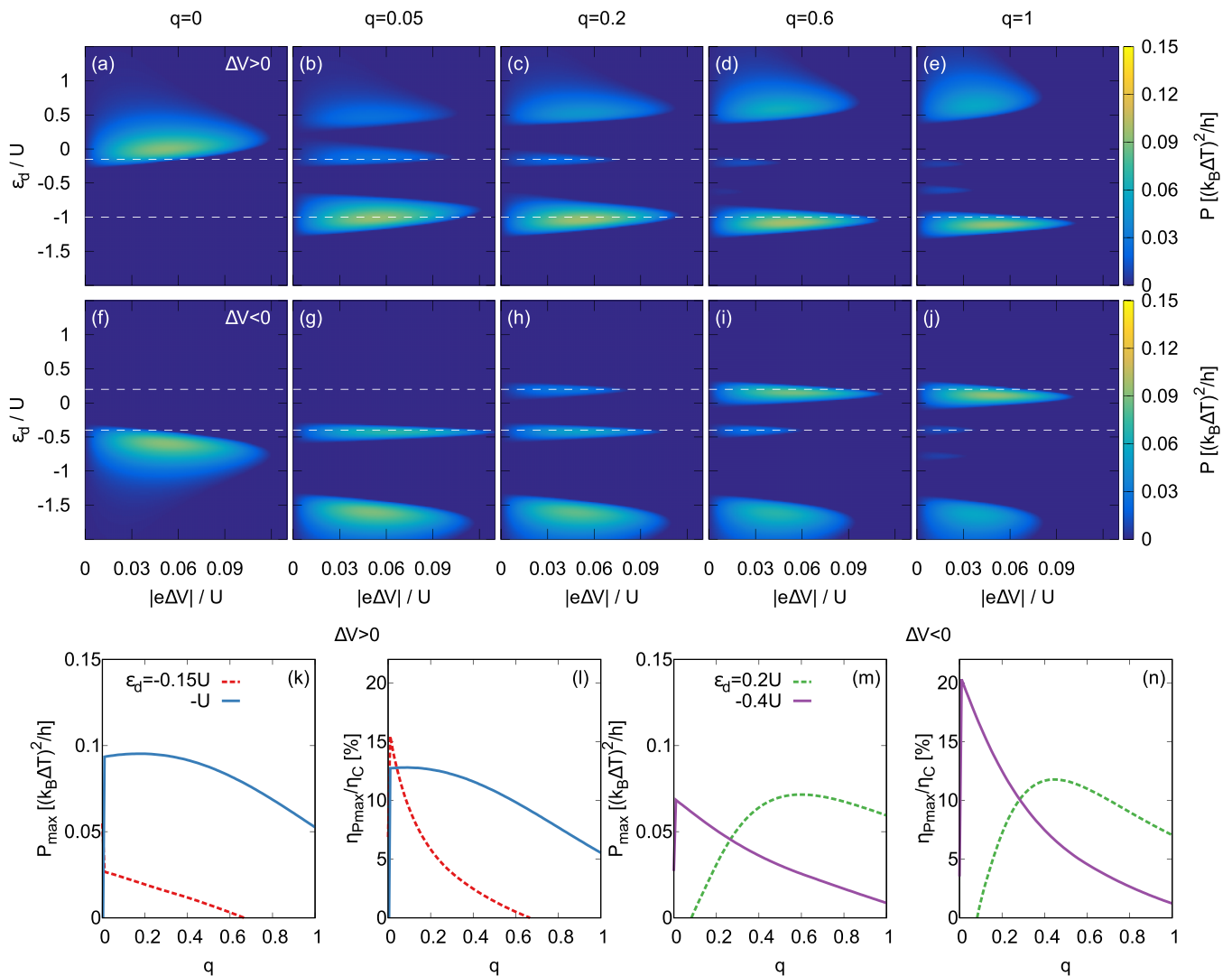
FIG. 8. Power, P, (a)–(j), as functions of the dot's energy level, ε_d, and applied bias voltage, $|e|\Delta V$, calculated for indicated values of the parameter q and $\Delta V > 0$ (a)–(e) and $\Delta V < 0$ (f)–(j). Maximal power, $P_{\max}$, and normalized efficiency at maximal power, $\eta_{P_{\max}}$, as a function of the parameter q for indicated dot's energy levels [marked also by the white dashed lines in (a) to (j)] and for $\Delta V > 0$, (k), (l), and $\Delta V < 0$, (m), (n). Other parameters: $p_L = p_R = 1$, $g\mu_B B = 0.6U$, $k_B T = k_B T_R = 0.5\Gamma$, $U = 10\Gamma$, and $\Delta T = 2T$.

of the spin-orbit coupling, one can tune the dot's energy level to reach the maximal power.

Due to the Zeeman splitting of the dot's level, the temperature dependence of electric and thermoelectric coefficients is more complex than in the absence of magnetic field. This temperature dependence of electric conductance, thermopower, and power factor for $p_L = p_R = 1$ is shown in Fig. 7 for indicated values of q and two values of the dot's energy level, $\varepsilon_d = 0.1U$ and $\varepsilon_d = -0.8U$. From Fig. 6(b), it follows that both these energies are in the vicinity of the peaks associated with the Rashba-induced channels, where the dependence on q is quite significant. This leads to a nontrivial dependence of the electric conductance, thermopower, and power factor on temperature. Physical origin of this behavior is similar to that presented already in the case of zero magnetic field, so we will not describe it in more detail.

Finite Zeeman splitting of the dot's energy level leads to additional peaks in power—similarly as it leads to the additional peaks in other transport/thermoelectric quantities

discussed above. The power generated in the system under consideration in the presence of external magnetic field is shown in Figs. 8(a)–8(j). The upper row in Figs. 8(a)–8(e) corresponds to $\Delta V > 0$, while the second row, Figs. 8(f)–8(j), corresponds to $\Delta V < 0$. For $q = 0$, the power spectrum shown in Figs. 8(a) and 8(f) for $\Delta V > 0$ and $\Delta V < 0$, respectively, is similar to the corresponding one in the absence of external magnetic field, i.e., it exhibits a single peak due to a single active spin channel only, which, however, is shifted toward the lower bare dot's energy level. This is because transport occurs through the $\varepsilon_\uparrow$ component of the Zeeman spin-split dot's level.

As in the case of zero magnetic field, the Rashba spin-flip tunneling for $q > 0$ opens the second spin channel for electronic transport through the quantum dot. Moreover, it also leads to interference effects (Fano antiresonance). For $q > 0$, the power shown in Figs. 8(b)–8(e) for $\Delta V > 0$ and in Figs. 8(g)–8(j) for $\Delta V < 0$ can be generated in broader ranges of the voltage and dot's level energy, in contrast to the case of $q = 0$, where only a single transport channel is
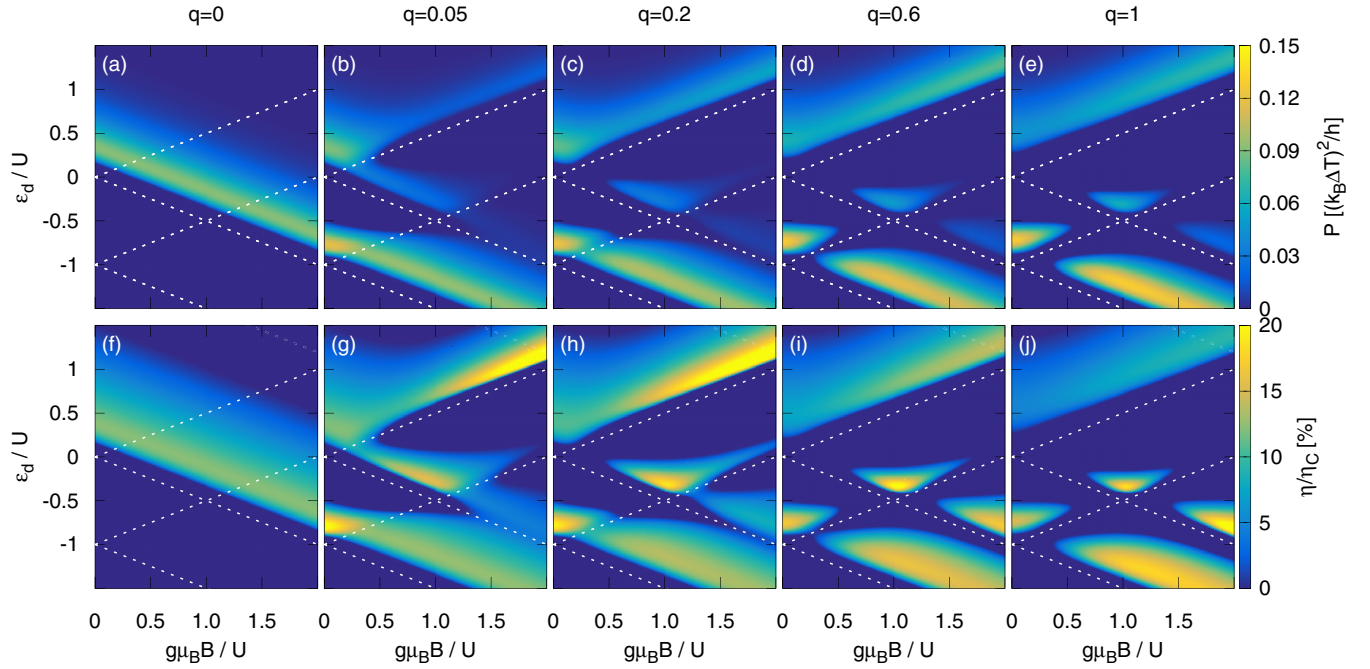
FIG. 9. Power, P, (a)–(e), and normalized efficiency, η/η_C, (f)–(j), as functions of the dot's energy level, ε_d, and magnetic field, $g\mu_B B$, for indicated values of parameter q. Other parameters: $p_L = p_R = 1$, $k_B T = 0.5\Gamma$, $U = 10\Gamma$, $e\Delta V = -0.05U$, and $\Delta T = 2T$. White dotted lines represent spin-dependent energy levels, $\varepsilon_\uparrow$ and $\varepsilon_\downarrow$.

open. The broadest voltage range where the power can be generated (maximal blocking voltage) occurs for small spin-orbit coupling (small q), where the Fano effect is relatively strong. Indeed, as shown in Fig. 6(b) for the linear response regime, the Fano antiresonance becomes less pronounced with increasing q.

The maximal power and the corresponding efficiency are shown in Figs. 8(k)–8(m) for selected positions of the dot's energy level and both voltage polarities. For $\Delta V > 0$, there is a rapid onset of the power due to activation of the spin-↓ channel and appearance of the antiresonance for $\varepsilon_d = -U$. In contrast, maximal power obtained when the transport occurs through spin-↑ channel vanishes quickly with increasing q due to increasing separation between the spin-↑ and spin-↓ levels.

The efficiency corresponding to maximal power, on the other hand, is the largest for the spin-↑ channel and small q. This is due to a small heat current flowing into the dot. However, the corresponding maximal efficiency rapidly decreases with increasing q since the power is no longer generated in this channel. In turn, the efficiency at maximal power in the Rashba-induced channel follows the q-dependence of the maximal power, as the dot's energy for which the generated power is maximal shifts toward lower values with increasing q. Similarly, the maximal power and the corresponding efficiency for $\Delta V < 0$, shown in Figs. 8(m) and 8(n), respectively, decay more quickly in the case of spin-↑ channel than for spin-↓ one.

The power generated in the system as well as the corresponding efficiency remarkably depend on the strength of magnetic field, as shown in Fig. 9 for the bias voltage, roughly corresponding to maximal values of the power and efficiency shown in Fig. 8, i.e., $|e|\Delta V = 0.05U$. For $q = 0$, the power and efficiency shown in Figs. 9(a) and 9(f), are roughly constant

with respect to magnetic field. However, the dot's energy level, for which the heat-to-work conversion occurs, depends linearly on magnetic field, as the transport occurs through the single spin-↑ level.

For $q > 0$, the spin-↓ channel is activated due to finite RSOC. This activation leads to complex interplay between the effects due to external magnetic field, RSOC, and Coulomb interaction. When the strength of spin-orbit coupling increases, the power shown in Figs. 9(b)–9(e) can be generated when the energy of spin-↓ electron overcomes the Coulomb blockade. For small q, the power is generated mostly through the spin-↑ channel. There is, however, relatively weak spin-↓ transport through the interference-induced resonant channel. With increasing q, the contribution of spin-↓ carriers increases as well, which results in an enhanced power generated in this channel, especially for large magnetic fields, when the spin-dependent energy levels are well separated. The corresponding efficiency, shown in Figs. 9(g)–9(j), for small q is the largest when the transport occurs through the interference-induced resonant ↓ channel, as the heat current flowing in this channel is smaller than that in the ↑ one. Consequently, an increase in q results in a larger contribution due to spin-↓ carriers, i.e., greater heat current, and thus in a decrease in efficiency. This indicates that the strength of RSOC should be relatively small to ensure larger efficiency.

IV. SUMMARY

In summary, we have analyzed a heat engine based on a quantum dot connected to half-metallic ferromagnetic leads. Both spin-conserving and spin-flip tunneling processes between the dot and electrodes were taken into account. The latter occur due to Rashba spin-orbit interaction. Basic parameters of

the engine, such as power and efficiency, can then be modulated not only by properties of the dot itself, such as position of the energy level or Coulomb correlation parameter, but also by RSOC. The latter, in principle, can be controlled by an external electric field.

A particularly interesting case occurs when the ferromagnetic leads are fully spin polarized and have aligned magnetic moments (parallel configuration). Even though only electrons of one spin orientation are then present in the electrodes, the RSOC activates the dot's level of the opposite spin, so the

effects due to double occupancy (Coulomb blockade) play an important role. Moreover, this also leads to resonant effects, especially to the Fano-like interference, where the spin-$\downarrow$ channel takes the role of a resonant channel, while the spin-$\uparrow$ channel assumes the role of background channel. This, in turn, leads to an enhanced thermoelectric response of the system. Moreover, when an external magnetic field is applied to the system, the complex interplay between the effects due to spin-orbit coupling, magnetic field, and Coulomb interaction leads to spin-selective power generation.

[1] L. D. Hicks and M. S. Dresselhaus, Effect of quantum-well structures on the thermoelectric figure of merit, Phys. Rev. B **47**, 12727 (1993).

[2] M. S. Dresselhaus, G. Chen, M. Y. Tang, R. Yang, H. Lee, D. Wang, Z. Ren, J.-P. Fleurial, and P. Gogna, New directions for low-dimensional thermoelectric materials, Adv. Mater. **19**, 1043 (2007).

[3] G. D. Mahan and J. O. Sofo, The best thermoelectric, Proc. Natl. Acad. Sci. USA **93**, 7436 (1996).

[4] A. A. M. Staring, L. W. Molenkamp, B. W. Alphenaar, H. van Houten, O. J. A. Buyk, M. A. A. Mabesoone, C. W. J. Beenakker, and C. T. Foxon, Coulomb-blockade oscillations in the thermopower of a quantum dot, Europhys. Lett. **22**, 57 (1993).

[5] R. Scheibner, H. Buhmann, D. Reuter, M. N. Kiselev, and L. W. Molenkamp, Thermopower of a Kondo Spin-Correlated Quantum Dot, Phys. Rev. Lett. **95**, 176602 (2005).

[6] S. Fahlvik Svensson, A. I. Persson, E. A. Hoffmann, N. Nakpathomkun, H. A. Nilsson, H. Q. Xu, L. Samuelson, and H. Linke, Lineshape of the thermopower of quantum dots, New J. Phys. **14**, 033041 (2012).

[7] A. Svilans, A. M. Burke, S. Fahlvik Svensson, M. Leijnse, H. Linke, Nonlinear thermoelectric response due to energy-dependent transport properties of a quantum dot, Physica E **82**, 34 (2016).

[8] M. Krawiec and K. I. Wysokiński, Thermoelectric effects in strongly interacting quantum dot coupled to ferromagnetic leads, Phys. Rev. B **73**, 075307 (2006).

[9] R. Świrkowicz, M. Wierzbicki, and J. Barnaś, Thermoelectric effects in transport through quantum dots attached to ferromagnetic leads with noncollinear magnetic moments, Phys. Rev. B **80**, 195409 (2009).

[10] T. Rejec, R. Žitko, J. Mravlje, and A. Ramšak, Spin thermopower in interacting quantum dots, Phys. Rev. B **85**, 085117 (2012).

[11] I. Weymann and J. Barnaś, Spin thermoelectric effects in Kondo quantum dots coupled to ferromagnetic leads, Phys. Rev. B **88**, 085313 (2013).

[12] U. Fano, Effects of configuration interaction on intensities and phase shifts, Phys. Rev. **124**, 1866 (1961).

[13] M. Wierzbicki and R. Świrkowicz, Influence of interference effects on thermoelectric properties of double quantum dots, Phys. Rev. B **84**, 075410 (2011).

[14] P. Trocha and J. Barnaś, Large enhancement of thermoelectric effects in a double quantum dot system due to interference and Coulomb correlation phenomena, Phys. Rev. B **85**, 085408 (2012).

[15] V. M. García-Suárez, R. Ferradás, J. Ferrer, Impact of Fano and Breit-Wigner resonances in the thermoelectric properties of nanoscale junctions, Phys. Rev. B **88**, 235417 (2013).

[16] Ł. Karwacki and P. Trocha, Spin-dependent thermoelectric effects in a strongly correlated double quantum dot, Phys. Rev. B **94**, 085418 (2016).

[17] K. P. Wójcik and I. Weymann, Strong spin Seebeck effect in Kondo T-shaped double quantum dots, J. Phys.: Condens. Matter **29**, 055303 (2017).

[18] J. P. Ramos-Andrade, F. J. Peña, A. González, O. Ávalos-Ovando, and P. A. Orellana, Spin-Seebeck effect and spin polarization in a multiple quantum dot molecule, Phys. Rev. B **96**, 165413 (2017).

[19] M. T. Björk, C. Thelander, A. E. Hansen, L. E. Jensen, M. W. Larsson, L. Reine Wallenberg, and L. Samuelson, Few-electron quantum dots in nanowires, Nano Lett. **4**, 1621 (2004).

[20] P. Jarillo-Herrero, S. Sapmaz, C. Dekker, L. P. Kouwenhoven, and H. S. J. van der Zant, Electron-hole symmetry in a semiconducting carbon nanotube quantum dot, Nature **429**, 389 (2004).

[21] S. Sapmaz, P. Jarillo-Herrero, L. P. Kouwenhoven, and H. S. J. van der Zant, Quantum dots in carbon nanotubes, Semicond. Sci. Technol. **21**, S52 (2006).

[22] Y. A. Bychkov and E. I. Rashba, Properties of a 2D electron gas with a lifted spectrum degeneracy, JETP Lett. **39**, 78 (1984).

[23] D. Bercioux and P. Lucignano, Quantum transport in Rashba spin-orbit materials: A review, Rep. Prog. Phys. **78**, 106001 (2015).

[24] F. Kuemmeth, S. Ilani, D. C. Ralph, and P. L. McEuen, Coupling of spin and orbital motion of electrons in carbon nanotubes, Nature **452**, 448 (2008).

[25] G. A. Steele, F. Pei, E. A. Laird, J. M. Jol, H. B. Meerwaldt, and L. P. Kouwenhoven, Large spin-orbit coupling in carbon nanotubes, Nat. Commun. **4**, 1573 (2013).

[26] S. Nadj-Perge, S. M. Frolov, E. P. A. M. Bakkers, and L. P. Kouwenhoven, Spin-orbit qubit in a semiconductor nanowire, Nature **468**, 1084 (2010).

[27] T. S. Jespersen, K. Grove-Rasmussen, J. Paaske, K. Muraki, T. Fujisawa, J. Nygård, and K. Flensberg, Gate-dependent spin-orbit coupling in multielectron carbon nanotubes, Nat. Phys. **7**, 348 (2011).

[28] F. Mireles and G. Kirczenow, Ballistic spin-polarized transport and Rashba spin precession in semiconductor nanowires, Phys. Rev. B **64**, 024426 (2001).

[29] P. A. Orellana, M. Amado, and F. Domínguez-Adame, Fano-Rashba effect in quantum dots, Nanotechnology **19**, 195401 (2008).

[30] P. Stefański, Interplay between quantum interference and electron interactions in a Rashba system, J. Phys.: Condens. Matter **22**, 505303 (2010).

[31] J. Cayao, E. Prada, P. San-Jose, and R. Aguado, SNS junctions in nanowires with spin-orbit coupling: Role of confinement and helicity on the subgap spectrum, Phys. Rev. B **91**, 024514 (2015).

[32] J. Nitta, F. E. Meijer, and H. Takayanagi, Spin-interference device, Appl. Phys. Lett. **75**, 695 (1999).

[33] Q.-F. Sun, J. Wang, and H. Guo, Quantum transport theory for nanostructures with Rashba spin-orbital interaction, Phys. Rev. B **71**, 165310 (2005).

[34] Y.-S. Liu, X.-K. Hong, J.-F. Feng, and X.-F. Yang, Fano-Rashba effect in thermoelectricity of a double quantum dot molecular junction, Nanoscale Res. Lett. **6**, 618 (2011).

[35] Y.-S. Liu, F. Chi, X.-F. Yang, and J.-F. Feng, Pure spin thermoelectric generator based on a Rashba quantum dot molecule, J. Appl. Phys. **109**, 053712 (2011).

[36] F. L. Curzon and B. Ahlborn, Efficiency of a Carnot engine at maximum power output, Am. J. Phys. **43**, 22 (1975).

[37] M. Esposito, K. Lindenberg, and C. Van den Broeck, Universality of Efficiency at Maximum Power, Phys. Rev. Lett. **102**, 130602 (2009).

[38] M. Esposito, R. Kawai, K. Lindenberg, and C. Van den Broeck, Efficiency at Maximum Power of Low Dissipation Carnot Engines, Phys. Rev. Lett. **105**, 150603 (2010).

[39] M. Esposito, R. Kawai, K. Lindenberg, and C. Van den Broeck, Quantum-dot Carnot engine at maximum power, Phys. Rev. E **81**, 041106 (2010).

[40] N. Nakpathomkun, H. Q. Xu, and H. Linke, Thermoelectric efficiency at maximum power in low-dimensional systems, Phys. Rev. B **82**, 235428 (2010).

[41] M. Esposito, N. Kumar, K. Lindenberg, and C. Van den Broeck, Stochastically driven single-level quantum dot: A nanoscale finite-time thermodynamic machine and its various operational modes, Phys. Rev. E **85**, 031117 (2012).

[42] B. Szukiewicz and K. I. Wysokiński, Quantum dot as spin current generator and energy harvester, Eur. Phys. J. B **88**, 112 (2015).

[43] K. Yamamoto and N. Hatano, Thermodynamics of the mesoscopic thermoelectric heat engine beyond the linear-response regime, Phys. Rev. E **92**, 042165 (2015).

[44] M. Josefsson, A. Svilans, A. M. Burke, E. A. Hoffmann, S. Fahlvik, C. Thelander, M. Leijnse, and H. Linke, Nat. Nanotech. (2018), doi: 10.1038/s41565-018-0200-5.

[45] O. Entin-Wohlman, Y. Imry, and A. Aharony, Three-terminal thermoelectric transport through a molecular junction, Phys. Rev. B **82**, 115314 (2010).

[46] H. Thierschmann, R. Saánchez, B. Sothmann, F. Arnold, C. Heyn, W. Hansen, H. Buhmann, and L. W. Molenkamp, Three-terminal energy harvester with coupled quantum dots, Nat. Nanotech. **10**, 854 (2015).

[47] B. Sothmann and M. Büttiker, Magnon-driven quantum-dot heat engine, Euro. Phys. Lett. **99**, 27001 (2012).

[48] C. Bergenfeldt, P. Samuelsson, B. Sothmann, C. Flindt, and M. Büttiker, Hybrid Microwave-Cavity Heat Engine, Phys. Rev. Lett. **112**, 076803 (2014).

[49] F. Mazza, R. Bosisio, G. Benenti, V. Giovannetti, R. Fazio, and F. Taddei, Thermoelectric efficiency of three-terminal quantum thermal machines, New J. Phys. **16**, 085001 (2014).

[50] K. Yamamoto, O. Entin-Wohlman, A. Aharony, and N. Hatano, Efficiency bounds on thermoelectric transport in magnetic fields: The role of inelastic processes, Phys. Rev. B **94**, 121402 (2016).

[51] A. V. Timofeev, M. Helle, M. Meschke, M. Möttönen, and J. P. Pekola, Electronic Refrigeration at the Quantum Limit, Phys. Rev. Lett. **102**, 200801 (2009).

[52] D. Venturelli, R. Fazio, and V. Giovannetti, Minimal Self-Contained Quantum Refrigeration Machine Based on Four Quantum Dots, Phys. Rev. Lett. **110**, 256801 (2013).

[53] J. P. Pekola, J. V. Koski, and D. V. Averin, Refrigerator based on the Coulomb barrier for single-electron tunneling, Phys. Rev. B **89**, 081309 (2014).

[54] J. P. Pekola, Towards quantum thermodynamics in electronic circuits, Nat. Phys. **11**, 118 (2015).

[55] P. Strasberg, G. Schaller, T. Brandes, and M. Esposito, Thermodynamics of a Physical Model Implementing a Maxwell Demon, Phys. Rev. Lett. **110**, 040601 (2013).

[56] V. Kashcheyevs, A. Schiller, A. Aharony, and O. Entin-Wohlman, Unified description of phase lapses, population inversion, and correlation-induced resonances in double quantum dots, Phys. Rev. B **75**, 115313 (2007).

[57] Ł. Karwacki, P. Trocha, and J. Barnaś, Spin-dependent thermoelectric properties of a Kondo-correlated quantum dot with Rashba spin-orbit coupling, J. Phys.: Condens. Matter **25**, 505305 (2013).

[58] G. Benenti, G. Casati, K. Saito, and R. S. Whitney, Fundamental aspects of steady-state conversion of heat to work at the nanoscale, Phys. Rep **694**, 1 (2017).